

ORIGINAL RESEARCH ARTICLE

A Mechanics-Based Phase-Field Model and Finite Element Simulations for Microstructure Evolution during Solidification of Ti-6Al-4V

Farhad Boorani Koopaei, Mahdi Javanbakht, and Mohammad Silani

Submitted: 7 June 2023 / Revised: 5 January 2024 / Accepted: 7 February 2024 / Published online: 26 March 2024

In this paper, a mechanics-based phase-field model at the microscale is introduced for microstructure evolution during solidification. The couple phase-field model consists of Allen–Cahn equation for phase order parameter, Cahn–Hilliard equation for composition, heat conduction and elasticity equations. The introduced elastic energy allows for volumetric inelastic strains due to melting/solidification as well as a thermodynamically consistent solid–melt interface stress and consequently, residual stresses during solidification at the microscale and deformation can be captured. The computational microcell is considered at the melt–solid interface and the temperature as a time dependent function is used for its boundary conditions to solve the coupled phase-field model. Using COMSOL FE code, examples of columnar growth are studied. As result, the suppressive effect of elastic driving forces and the reduction in solidification rate, due to the volumetric inelastic strains, on solidification are revealed. The inelastic surface stress, concentrated inside the interface, can change the morphology of solidified structure but does not show a remarkable effect on the solidification rate. The thermal strain was included which reduced the effect of volumetric transformation strain and consequently, the internal stresses near constrained regions were decreased. The effect of undercooling was studied which showed that increasing the undercooling increased the temperature gradient in the vertical direction and near the interface and solidification rate and significantly changed the morphology of solidified structure, as a homogeneous growth was resolved for larger undercooling while a columnar growth was obtained for smaller undercooling. Solidification was studied under mechanical loading which showed external loading changes the stress distribution and magnitude and the morphology of solidified structure. Effect of an inclusion on solidification was also investigated. The inclusion represented a more homogeneous distribution of stress and temperature with different magnitudes compared to the rest of the sample, creating a directional solidification toward the inclusion.

Keywords elastic energy, laser cladding process, microstructure, phase-field, residual stress, solidification

1. Introduction

Additive manufacturing (AM) refers to processes which make parts in a layer-layer manner. Direct energy deposition (DED), selective laser melting (SLM) and electron beam melting (EBM) are the most common methods used for metal AM (Ref 1-3). Recent advances demonstrate the abilities and

potentials of the AM for fabrication of complex geometries, near net shape manufacturing, optimum use of material and cost reduction of expensive tools (Ref 4, 5). Dendritic growth during the solidification in alloys influences the microstructure and mechanical properties such as strength, hardness, creep resistance, fracture resistance and so on (Ref 6, 7). For the design and optimization of AM fabricated components, many researchers investigated process-structure-property relations in AM processes. Trial and error experiments to relate the AM process parameters to specific mechanical properties such as the combination of high strength and good ductility are the first investigations in this field (Ref 8).

In addition, different numerical methods have been performed to study the microstructure of AM fabricated components. Each method represents some degree of accuracy and a specific length scale (Ref 9) (Fig. 1). In some cases, multiscale procedures consisting of micro- and macro-simulations have been utilized to accurately include scale dependent material and model parameters.

The first study of grain texture formation at the microscale was conducted using the Kinetic Monte Carlo (KMC) and the cellular automaton (CA) methods. Rodgers et al and Wei et al used the KMC method to simulate the 3D grain evolution during the AM process for Ti-6Al-4V and AL 1050A, respectively (Ref 10, 11). Carozzani et al. used the CA method

This invited article is part of a special topical issue of the *Journal of Materials Engineering and Performance* on Residual Stress Analysis: Measurement, Effects, and Control. The issue was organized by Rajan Bhambroo, Tenneco, Inc.; Lesley Frame, University of Connecticut; Andrew Payzant, Oak Ridge National Laboratory; and James Pineault, Proto Manufacturing on behalf of the ASM Residual Stress Technical Committee.

Farhad Boorani Koopaei, Mahdi Javanbakht, and Mohammad Silani, Department of Mechanical Engineering, Isfahan University of Technology, Isfahan 84156-83111, Iran. Contact e-mail: javanbakht@iut.ac.ir.

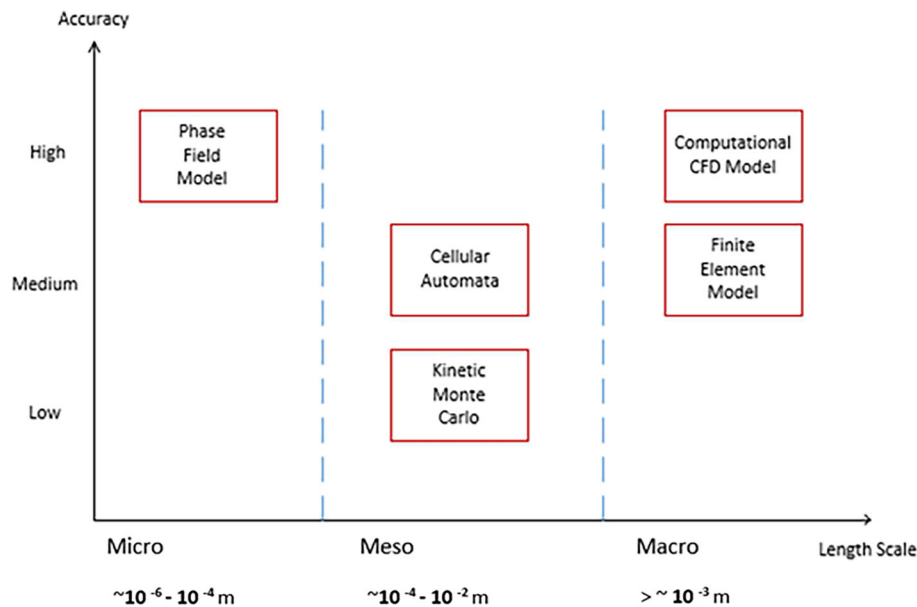


Fig. 1 Schematic diagram comparing different models in terms of length scale and accuracy

in couple with macro-thermal analysis using the finite element method to simulate the grain growth in directional solidification (Ref 12). Also, Li et al. used the CA method to simulate the melt pool in a multilayer AM product in couple with thermal history analysis using the finite volume (Ref 13). In general, the results of the CA method showed a good agreement with experimental results compared to those of the KMC method.

The phase-field (PF) method has been extensively used to capture the nano/microstructure evolution for a broad range of complex problems such as martensitic phase transformations (Ref 14), twinning (Ref 15, 16), crack growth (Ref 17), grain growth (Ref 18), dislocations (Ref 19, 20), voids (Ref 21) and melting/solidification (Ref 22, 23). The PF method is also one of the most accurate methods to simulate the cellular dendrite during AM processes at the microscale. Usually, it is combined with macro-level simulations due to the required model parameters. Ramirez et. al proposed a set of the PF equations consisting of the Allen–Cahn, Cahn–Hilliard and heat equations to simulate the binary alloy solidification with anti-trapping solute current with no kinetic effect (Ref 22). Also, Echebarria et al. advanced the Ramirez’s model to simulate the low speed directional solidification by substituting the heat equation with a temperature gradient with a given specific velocity within the PF equations (Ref 23).

Multiscale simulations have been known as an essential way to investigate AM processes. Acharya used computational fluid dynamics (CFD) to simulate the melt pool temperature and displacement field and resolved the dendrite evolution, segregation of dissolved element and primary dendrite arm spacing (PDAS) (Ref 24). Also, there are more relevant works which made a macroscale temperature study and linked it to the microscale PF analysis through boundary conditions or thermal gradients and resolved a more accurate dendritic growth by considering chemical and electrochemical effects, voids and impurities. The effect of temperature gradient is also investigated (Ref 7, 25–27). Cooling rate ($\dot{T}[K/s]$) is an import variable to determine the characteristics of microstructure which is the product of solidification growth rate ($R[m/s]$) and thermal gradient ($G[K/m]$). Increasing the thermal gradient increases the cooling rate at a constant growth rate, which leads

to a finer, more columnar structure with smaller spacing between the columnar dendrites.

Among, some works focused more on microscale simulations to capture phenomenological microstructure. Tourret et al. proposed a PF model to study the growth of 2D columnar dendritic grains and the effect of temperature gradient and grain crystallography on the selection of grain and orientations was considered. This model also has a novel nonlinear variable to enhance the numerical stability of equations for larger grid spacing (Ref 28). Park et al. investigated the microstructure growth considering the epitaxial effect of a previously built layer (Ref 29). Yang et al. presented multiscale simulations based on a macro-thermal fluid model and a PF model incorporating the classical nucleation theory and the initial grain structures of powder particles and substrate (Ref 30). Zhang et al. proposed a macro-PF model combined with a moving heat source to study the effect of particle features on defects and porosities of SLS products (Ref 31).

Effects of mechanics thorough elastic, viscoelastic or similar models in the PF models have been recently investigated revealing significant effects on the solidification kinetics, thermodynamics and morphology of microstructures. Liu et al. proposed a grain growth based PF model and elastoviscoplastic-fast Fourier transformation micromechanical model to investigate various morphologies such as columnar and equiaxed microstructures and columnar to equiaxed transition (Ref 32). Li et al. presented a PF model to integrate the relevant thermal fluid phenomena and the elastic structure response to describe the powder-substrate interaction during SLM process (Ref 33). The PF formulation including the deviatoric transformation strain is an advancement, which incorporated a promoting driving force for both melting and solidification and consequently, predicted a lower melting temperature (Ref 34, 35).

In this paper, a mechanics-based phase-field model at the microscale is proposed for the microstructure evolution during solidification which involves 4 sets of equations consisting of Allen–Cahn equation for the phase order parameter, Cahn–Hilliard equation for the alloy composition, heat equation and elasticity equations, while the previous main works (Ref 4, 7)

include only two of them, i.e., Allen–Cahn equation for the phase order parameter and Cahn–Hilliard equation for the alloy composition. They do not involve elasticity equations and their potential energy does not have the elastic part. Thus, they cannot capture the elastic/inelastic stress distribution and deformation, which are the key results of the current work. Moreover, the previous works do not involve the heat conduction equation and assume that the solid interface moves with a predefined velocity under an imposed thermal gradient.

2. Material and Methodology

2.1 Model Assumptions

The main assumptions of the model, which simplify the numerical solution but allow for the essential physical aspects of solidification are as the following (Ref 22, 23):

- The material properties are considered constant and equal for solid and liquid phases.
- “Anti-trapping” current is considered which is a solute flux from solid to liquid normal to the diffuse interface. This current can lead to precisely recover the local equilibrium at the interface and correct the solute distribution.
- The solute diffusion in the solid state is neglected due to the insignificant solid solute diffusion compared to liquid.
- The diffuse interface width is mesoscopic, i.e., it is about one order smaller than the radius of the interface curvature.
- Kinetic effects are negligible as for many alloys, solidified at small undercooling/supersaturation.

2.2 Phase-Field Model

The solution domain is solved for the main field variables consisting of the phase order parameter for the Allen–Cahn, the solute concentration for the Cahn–Hilliard, temperature for the heat conduction and displacements for the elasticity equations using the FE method by COMSOL Multiphysics. An initial periodic distribution of the columnar solidified structure is considered to study the progressive columnar growth.

The total free energy F can be introduced as:

$$F[\varphi, c, T] = \int f_{AB}(\varphi, c, T) dV \quad (\text{Eq 1})$$

where $f_{AB}(\varphi, c, T)$ denotes the bulk free energy density of a binary mixture of A and B atoms and c denotes the solute concentration of B. The bulk free energy density consists of the elastic (ψ^e), double well ($\check{\psi}^\theta$), thermal (ψ^θ), solute addition related (ψ^c) and gradient (ψ^∇) terms as:

$$f_{AB}(\varphi, c, T) = \psi^e + J\check{\psi}^\theta + \psi^\theta + \psi^c + J\psi^\nabla \quad (\text{Eq 2})$$

$$\psi^e = \frac{1}{2} \boldsymbol{\sigma}_e : \boldsymbol{\epsilon}_e = \frac{1}{2} (\boldsymbol{\sigma} - \boldsymbol{\sigma}_{in}) : (\boldsymbol{\epsilon} - \boldsymbol{\epsilon}_{in}) \quad (\text{Eq 3})$$

$$\check{\psi}^\theta = \check{\psi}^\theta(\varphi, T_M) = H \left(-\frac{\varphi^2}{2} + \frac{\varphi^4}{4} \right) \quad (\text{Eq 4})$$

$$\psi^\theta = \left. \frac{\partial \check{\psi}^\theta(\varphi, T)}{\partial T} \right|_{T=T_M} \Delta T \quad (\text{Eq 5})$$

$$\psi^c = \frac{RT_M}{v_0} (c \ln c - c) + \bar{\epsilon} c + \bar{g}(\varphi) \frac{\Delta \epsilon}{2} c \quad (\text{Eq 6})$$

$$\psi^\nabla = \frac{\beta}{2} \left| \nabla \varphi \right|^2 \quad (\text{Eq 7})$$

where J is the deformation Jacobian, $\boldsymbol{\sigma}$ is the total stress tensor, $\boldsymbol{\sigma}_e$ is the elastic stress tensor, $\boldsymbol{\epsilon}$ is the total strain tensor, $\boldsymbol{\epsilon}_e$ is the elastic strain tensor, T_M is the melting temperature, H is the barrier height, R is the universal gas constant, v_0 is the molar volume, $\bar{g}(\varphi)$ is a monotonously increasing function which satisfies $\bar{g}(\pm 1) = \pm 1$ with $\varphi = +1$ ($\varphi = -1$) corresponding to solid (liquid), $\Delta \epsilon \equiv \epsilon_s - \epsilon_l$ and β is the gradient energy coefficient (Ref 22, 23).

Based on the second thermodynamics law which leads to a thermodynamically consistent stress tensor and kinematic decomposition, the expressions for the surface stress and the strain tensor are (Ref 34):

$$\boldsymbol{\sigma}_{in} = \boldsymbol{\sigma}_{surface\ tension} = \left(\check{\psi}^\theta + \psi^\nabla \right) \mathbf{I} - \beta \nabla \varphi \otimes \nabla \varphi \quad (\text{Eq 8})$$

$$\boldsymbol{\epsilon}_{in} = \frac{1}{3} \epsilon_{0t} (1 - l(\varphi)) \mathbf{I} \quad (\text{Eq 9})$$

$$l(\varphi) = \frac{1}{4} (\varphi + 1)^2 (2 - \varphi) \quad (\text{Eq 10})$$

where ϵ_{0t} is the transformation volume strain and $l(\varphi)$ is an interpolation function for the material properties between the solid ($\varphi = +1$) and melt ($\varphi = -1$) phases with the following four conditions; $l(-1) = 0$, $l(+1) = 1$ and $\left. \frac{\partial l}{\partial \varphi} \right|_{\varphi=\pm 1} = 0$. If the difference between gradients in the deformed and undeformed configurations is neglected, i.e., $J = 1$, surface stress $\boldsymbol{\sigma}_{in}$ (Eq. 8) disappears. Since $J = 1 + \mathbf{I} : \boldsymbol{\epsilon}_\theta$, then $dJ/d\boldsymbol{\epsilon} = \mathbf{I}$. Thus, multiplying J to the double well $\check{\psi}^\theta$ and the gradient energy ψ^∇ creates the term $(\check{\psi}^\theta + \psi^\nabla) \mathbf{I}$ and the difference between gradients in the deformed and undeformed configurations retains the term $-\beta \nabla \varphi \otimes \nabla \varphi$ for the surface stress. This is valid for both large and small strain theories (Ref 36). With definition of the bulk free energy per unit volume (F), the coupled system of equations is defined as

$$\frac{\partial \varphi}{\partial t} = -J^{-1} K_\varphi \frac{\delta F}{\delta \varphi} \quad (\text{Eq 11})$$

$$\frac{\partial c}{\partial t} = \nabla \cdot \left(J^{-1} K_c \frac{\delta F}{\delta c} - \vec{j}_{at} \right) \quad (\text{Eq 12})$$

$$\frac{\partial T}{\partial t} = \alpha \nabla^2 T + \frac{L}{2c_p} \frac{\partial \varphi}{\partial t} \quad (\text{Eq 13})$$

$$0 = \nabla \cdot \left(\boldsymbol{\sigma}_{in} + \mathbf{C}_{(E,v)} : \left(\frac{1}{2} \left[(\nabla \vec{u})^T + \nabla \vec{u} \right] - \boldsymbol{\epsilon}_{in} \right) \right) + \mathbf{f}_v \quad (\text{Eq 14})$$

where K_φ and K_c are constant and \vec{j}_{at} is the anti-trapping current, α is thermal diffusivity, L is latent heat and c_p is the specific heat at constant pressure, \mathbf{f}_v is the bulk force and

$C_{(E,v)}$ is the fourth-order elastic tensor. To simplify the numerical work, the dimensionless parameters u and U are defined as:

$$u = \ln\left(\frac{2c/c_\infty}{1+k-(1-k)\varphi}\right) \quad (\text{Eq 15})$$

$$U = \frac{\exp(u) - 1}{1-k} \quad (\text{Eq 16})$$

where c_∞ is the initial melt concentration and k is the equilibrium partition coefficient; thus, equations (11) and (12) can be extended as the following as:

$$\begin{aligned} \tau \frac{\partial \varphi}{\partial t} = & W^2 \nabla^2 \varphi + \varphi - \varphi^3 \\ & - \lambda \dot{g}_{(\varphi)} \left(\frac{T - T_M - mc_\infty}{L/c_p} + Mc_\infty U \right) - \frac{1}{JH} \frac{\partial \psi^e}{\partial \varphi} \end{aligned} \quad (\text{Eq 17})$$

$$\begin{aligned} \frac{1+k}{2} \frac{\partial U}{\partial t} = & \vec{\nabla} \cdot \left(D \frac{1-\varphi}{2} \vec{\nabla} U + \frac{W}{2\sqrt{2}} \left[1 + (1-k)U \frac{\partial \varphi}{\partial t} \frac{\vec{\nabla} \varphi}{|\vec{\nabla} \varphi|} \right] \right) \\ & + \frac{1}{2} \frac{\partial}{\partial t} \{ \varphi [1 + (1-k)U] \} \end{aligned} \quad (\text{Eq 18})$$

where τ is the characteristic time, W is the interface width, λ is the coupling constant, $\dot{g}_{(\varphi)} = (1 - \varphi^2)^2$, m is the liquidus slope of the dilute alloy phase diagram and M is the scaled magnitude of the liquidus slope. Ti-6Al-4V is used as the material under study in this research. Titanium and its alloys, specially Ti-6Al-4V is widely used in automotive, aerospace, energy and biomedical applications due to their superior physical properties like excellent strength-to-weight ratio, bio compatibility and corrosion resistance (Ref 7, 37, 38). Ti-6Al-4V is a two-phase alloy composed of β phase with a BCC structure and α phase with a hcp structure (Ref 39). Al stabilizes α which imparts the solid solution strengthening

and V stabilizes β which improves the ductility and fatigue properties (Ref 38). Table 1 lists some of the physical parameters used in the simulations (Ref 7, 37, 40, 41).

2.3 Numerical Procedure

There are three characteristic parameters in the phase-field model consisting of the coupling constant λ , interface width W_0 and characteristic time τ_0 that control the simulation physics and can be related to physical units as

$$d_0 = a_1 W_0 / \lambda \quad (\text{Eq 19})$$

$$\tilde{D} = a_2 \lambda \quad (\text{Eq 20})$$

$$\tau_0 = a_2 \lambda W_0^2 / D \quad (\text{Eq 21})$$

where $a_1 = 0.8839$ and $a_2 = 0.6267$ are constants, d_0 is the capillary length and \tilde{D} is the scaled diffusivity (Ref 22). Table 2 shows the complete set of the phase-field model input parameters.

The solution domain is a rectangular cell with the size of $40.8 \times 40 \mu\text{m}^2$. Zero flux for the phase is applied at all the boundaries. Zero flux condition for the phase order parameter means that the surface energy does not change over the sample and surface induced solidification/melting does not occur. The dimensionless concentration variable has zero value at the bottom and top sides and zero flux at the lateral sides. Also, zero displacement is applied at the bottom side and other sides are free. Since the Lewis number is 1, the heat conduction occurs slowly and it is reasonable to consider a uniform (or homogenous) temperature distribution with a semi-equilibrium magnitude at the boundaries. Here, the temperature is chosen as 1900 K and it descends slightly during the simulation.

COMSOL code was used to solve the coupled system of equations for alloy solidification. Allen–Cahn, Cahn–Hilliard and Heat conduction equations were implemented in the PDE coefficient form application and the elasticity equations were implemented in Structural Mechanics-Solid mechanics application. In addition, adjustable time step with an initial value of $0.8 \mu\text{s}$ was used which allows for a faster and easier convergence. The iterative segregated solver was employed which works based on an iterative algorithm for nonlinear problems. It does not solve for all the unknowns at one time. Instead, it subdivides the problem into two or more segregated steps which are solved sequentially within a single iteration;

Table 1 Thermo-physical properties of Ti-6Al-4V (Ref 7, 37, 40-42)

Parameter	Symbol	Unit	Value
Liquid slope	m	K/%	-0.088
Melting point	T_M	K	1928
Specific heat	c_p	J/kg · K	759
Latent heat	L	J/kg	36500
Liquid Solutal diffusivity	D	m^2/s	$9.5\text{e}-9$
Equilibrium partition coefficient	k	...	0.838
Initial alloy concentration	C_0	%	10
Deformation Jacobean	J	...	1
Transformation volume strain	ϵ_{0t}	...	0.02
Elastic modulus	E	GPa	114
Poisson's ratio	ν		0.342
Density	ρ	kg/m^3	4430
Thermal expansion coefficient	α_{tr}	K^{-1}	$9.5\text{e}-6$

Table 2 Phase-field model parameters

Parameter	Symbol	Unit	Value
Interphase thickness	W_0	m	$1\text{e}-7$
Coupling constant	λ	...	6.3826
Characteristic time	τ_0	s	$4.2\text{e}-6$
Lewis number	$Le \equiv D/\alpha$...	1
Undercooling	ΔT_M	K	328

thus, a less memory is required and an easier convergence is obtained.

3. Results and Discussion

Evolution of the solidification microstructure, i.e., phase order parameter, concentration and temperature is presented in Fig. 2 for five different cases (a) without elastic energy, (b) with elastic energy and without inelastic surface stress and (c) with both elastic energy and inelastic surface stress and without thermal expansion and (d) with both elastic energy and thermal expansion and without inelastic surface stress and (e) with total elastic energy, thermal

expansion and inelastic surface stress. For an easier comparison, all the figures are plotted in the undeformed configuration. It is clearly visible that the inelastic surface stress and elastic energy create a negative driving force for solidification and consequently, suppress solidification and reduce its rate. The tensile stress at the interface tends to reduce the interface area and this effect is more pronounced for interfaces with larger curvatures, i.e., smaller radii; thus, the tensile stress leads to the shrinkage and disappearance of small melt islands. Hence, the elastic energy causes less porosity during solidification, resulting in a more uniform solidified region. The thermal strain leads to a less heterogeneous structure with less dendrites.

The solid phase fraction, defined as the ratio of the area of the solidified region to the initial area, is plotted for the above

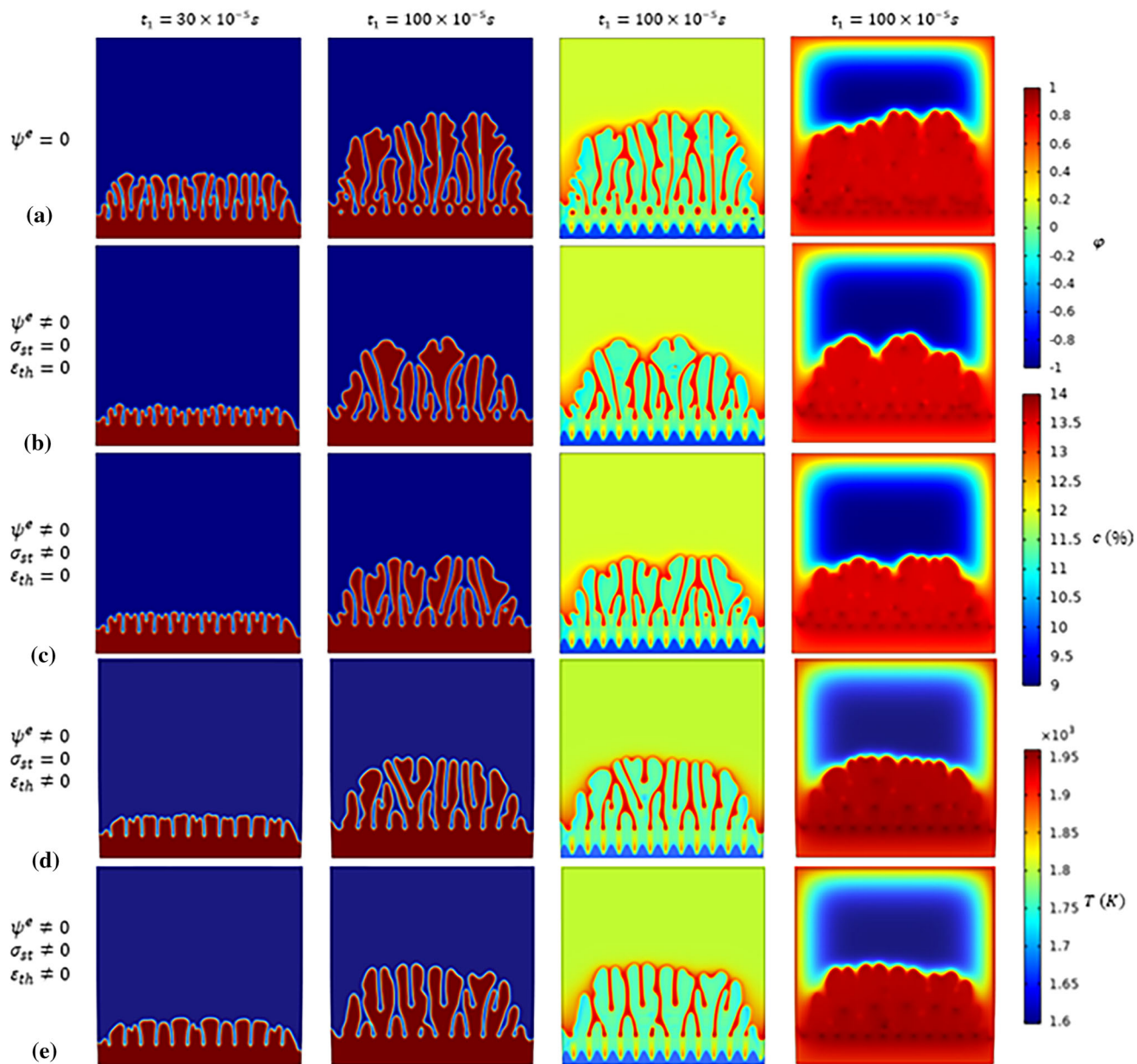


Fig. 2 Evolution of the phase order parameter, concentration and temperature for (a) without elastic energy, (b) with elastic energy and without inelastic surface stress and (c) with both elastic energy and inelastic surface stress and without thermal strain and (d) with both elastic energy and thermal expansion without inelastic surface stress and (e) with total elastic energy, thermal strain and inelastic surface stress

different cases in Fig. 3. As can be seen, the elastic energy reduces the solidification rate especially for the initial stage of growth. Also, the inelastic surface stress shows a small effect on the solidification rate. Note that even without external loading, the mechanical effects are significant due to the internal stresses caused by the volumetric inelastic strains.

Since the thermal diffusivity is limited, the heat conduction occurs at a limited rate which makes the thermal interface thicker, allowing for equiaxial or columnar/equiaxial structure. Note that the elastic energy reduces the rate of change in temperature since it reduces the solidification rate but it does not practically affect the temperature gradient values. The distribution of hydrostatic stress with inelastic surface stress and without it and the distribution of inelastic surface stress at the vertical direction are presented in the deformed configuration in Figs. 4 and 7, respectively. The inelastic surface stress is found one order smaller than the hydrostatic stress and this is trivial compared to the existing investigations on inelastic surface stress effects (Ref 43). A very important point is that

due to the negative volumetric transformation strain of solidification, the solidified regions are shrunk and represent positive stress; while the neighboring melt regions are expanded and represent negative stress (Fig. 4). Also, far from the solidified regions and near the lateral and upper sides, the stress reduces to zero due to the boundary effect. As shown in Fig. 5, the effect of thermal strain on the stress distribution can be significant. It causes a lower tension on the solid phase since in contrast to the negative transformation strain, it represents positive inelastic strain; thus, compared to Fig. 4, it reduces the effect of the transformation strain which leads to a different morphology and a lower solidification rate. The thermal strain is known to create stress in the regions where displacement is constrained. Hence, the effect of thermal strain on the stress reduction is more pronounced near the lower boundary since it is fixed while the other boundaries are free. As shown in Fig. 5, a stress reduction of 50% is obtained near the lower boundary due to the thermal strain.

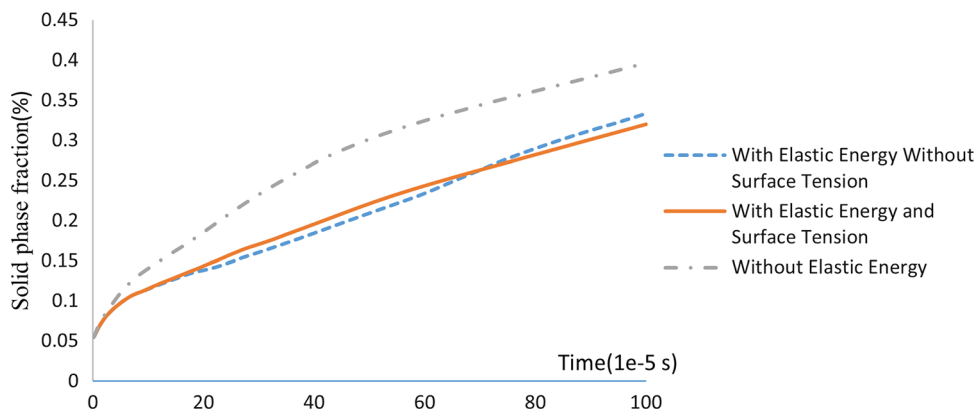


Fig. 3 Solid phase fraction vs. time

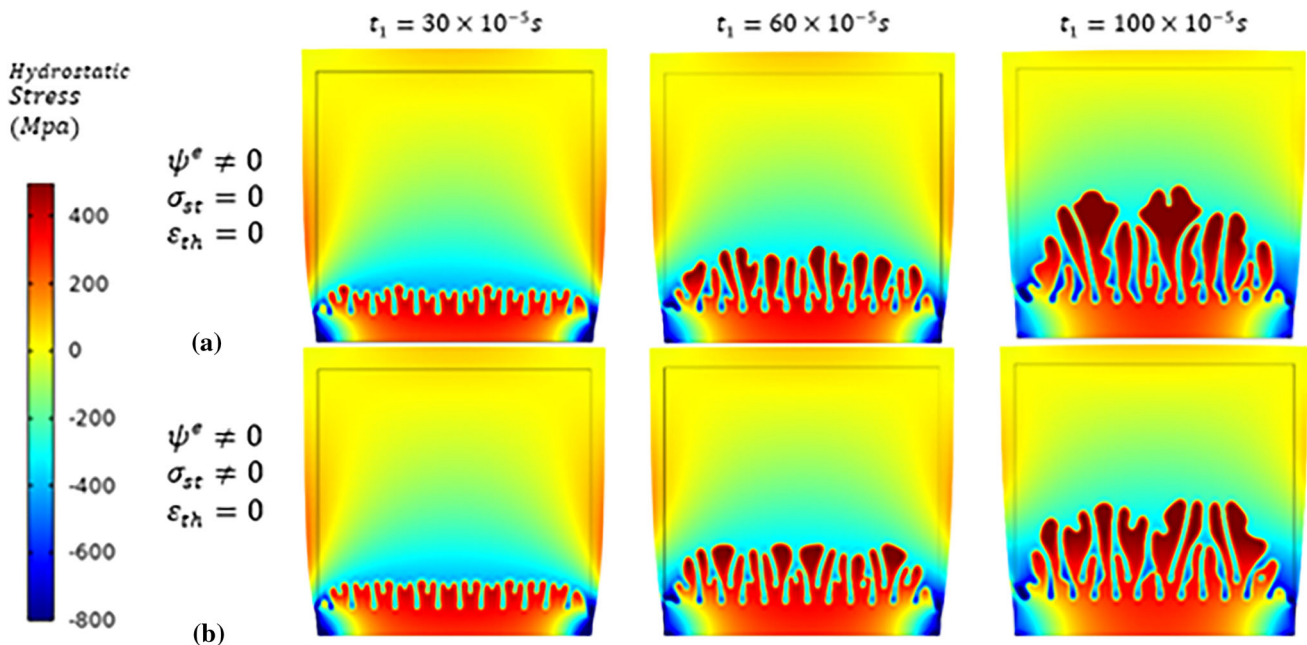


Fig. 4 Distribution of hydrostatic stress (without thermal expansion): (a) for the case without inelastic surface stress and (b) for the case including inelastic surface stress

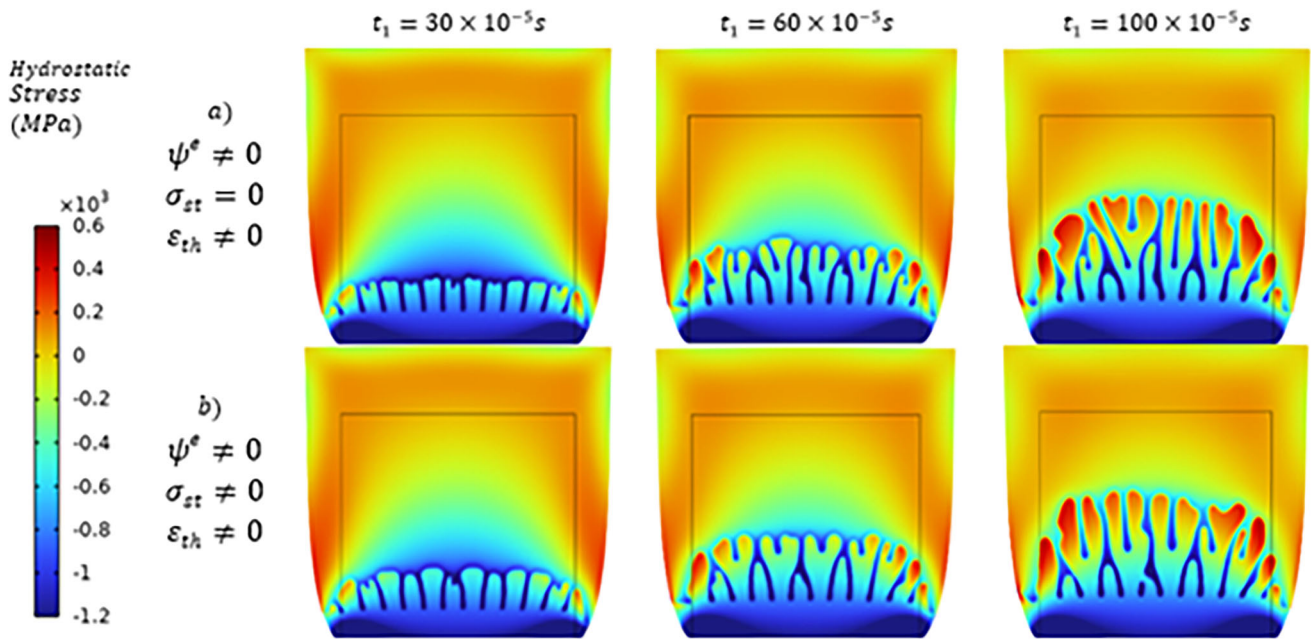


Fig. 5 Distribution of hydrostatic stress (with thermal expansion): (a) for the case without inelastic surface stress, (b) for the case including inelastic surface stress

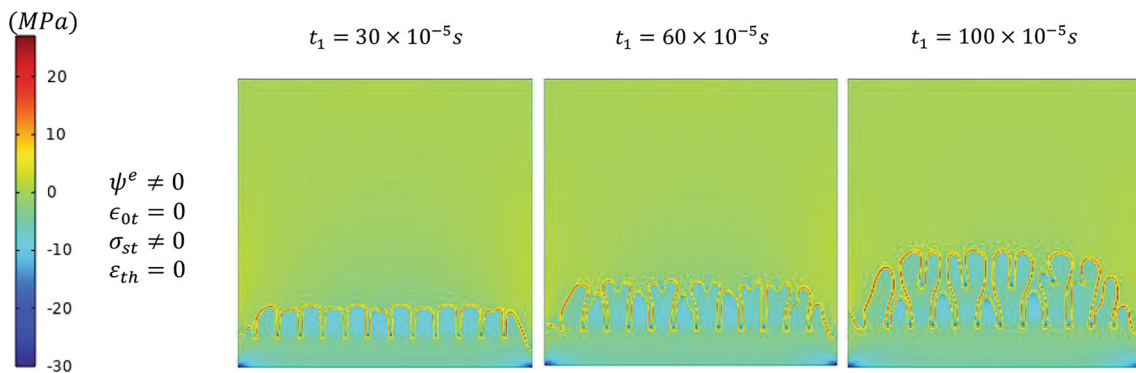


Fig. 6 Distribution of hydrostatic stress without volumetric transformation strain

It is worthy to note that the effect of inelastic surface stress is pronounced for smaller volumetric transformation strains. If one neglects the volumetric strain due to the solidification, the deformation disappears and the stress value significantly decreases and becomes concentrated within the solid-melt interface region, as shown in Fig. 6. Consequently, the phase morphology becomes very close to the case without elastic energy (Fig. 7).

The effect of undercooling, as a crucial parameter in determining the microstructure evolution, is also investigated. Change in the undercooling magnitude changes the thermal gradient and growth rate and consequently, the microstructure morphology (Ref 5). Figure 8 represents the evolution of the microstructure and hydrostatic stress for three different undercooling magnitudes. As shown from Fig. 8a to c, increasing the undercooling increases the growth rate. It also significantly changes the morphology, as a homogeneous growth is resolved for larger undercooling of $\Delta T_M = 528K$ while a columnar

growth is obtained for smaller undercooling magnitudes of $\Delta T_M = 328$ and $528K$, in agreement with the data in (Ref 5). The stress distribution is also more homogeneous for larger undercooling. The maximum temperature gradient along the vertical direction (time period of $1 \times 10^{-5}(s)$ to $5 \times 10^{-5}(s)$) varies in the range of 12×10^7 to 9×10^7 (K/m) for $\Delta T_M = 128K$, 20×10^7 to 9×10^7 (K/m) for $\Delta T_M = 328K$ and 30×10^7 to 10×10^7 (K/m) for $\Delta T_M = 528K$, which proves the thermal gradient increase as the undercooling increases.

The current mechanics based phase field model also allows for the study of solidification under mechanical loading. For instance, solidification is studied under three different hydrostatic stresses of $\sigma_{0h} = -200, 0$ and 200 MPa. As shown in Fig. 9, external loading changes the stress distribution and magnitude and consequently, the morphology. This is because external loading creates positive or negative transformation work which promote or suppress solidification. A larger

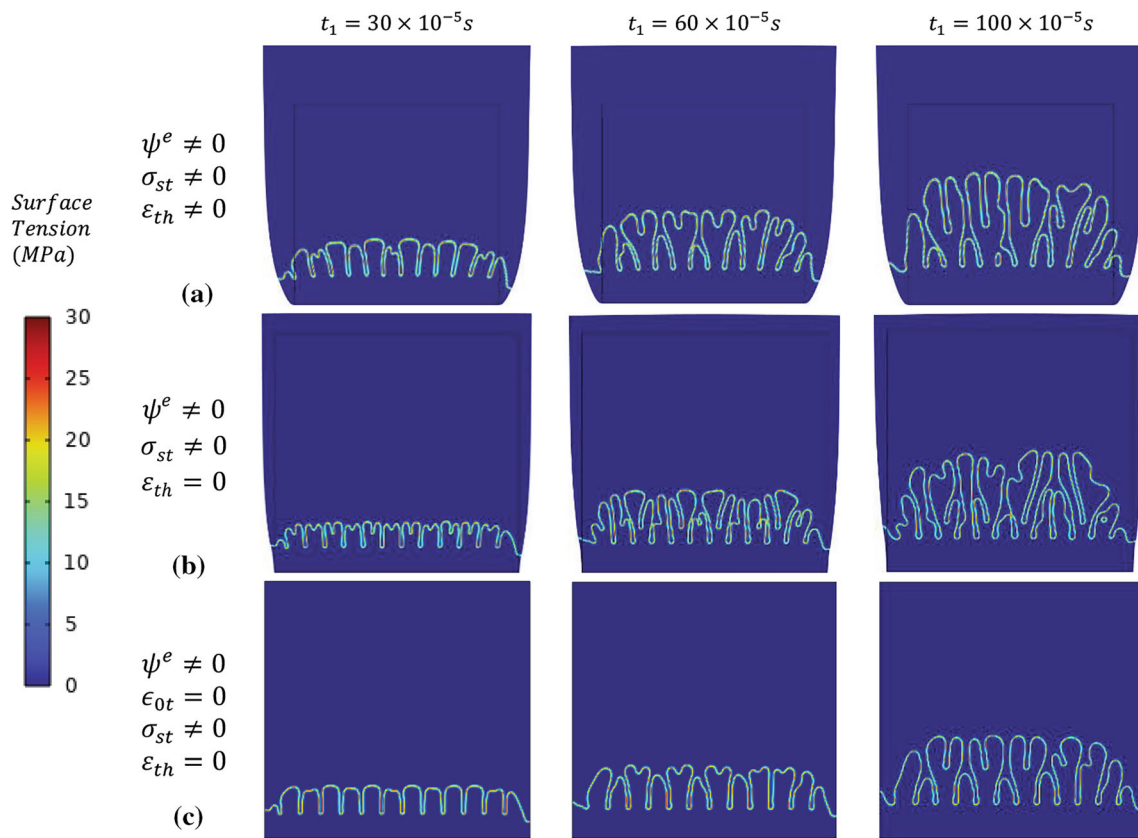


Fig. 7 Distribution of inelastic surface stress at the vertical direction a) for the case including volumetric transformation strain and thermal strain, b) for the case including volumetric transformation strain without thermal strain and c) for the case without volumetric transformation strain and thermal strain

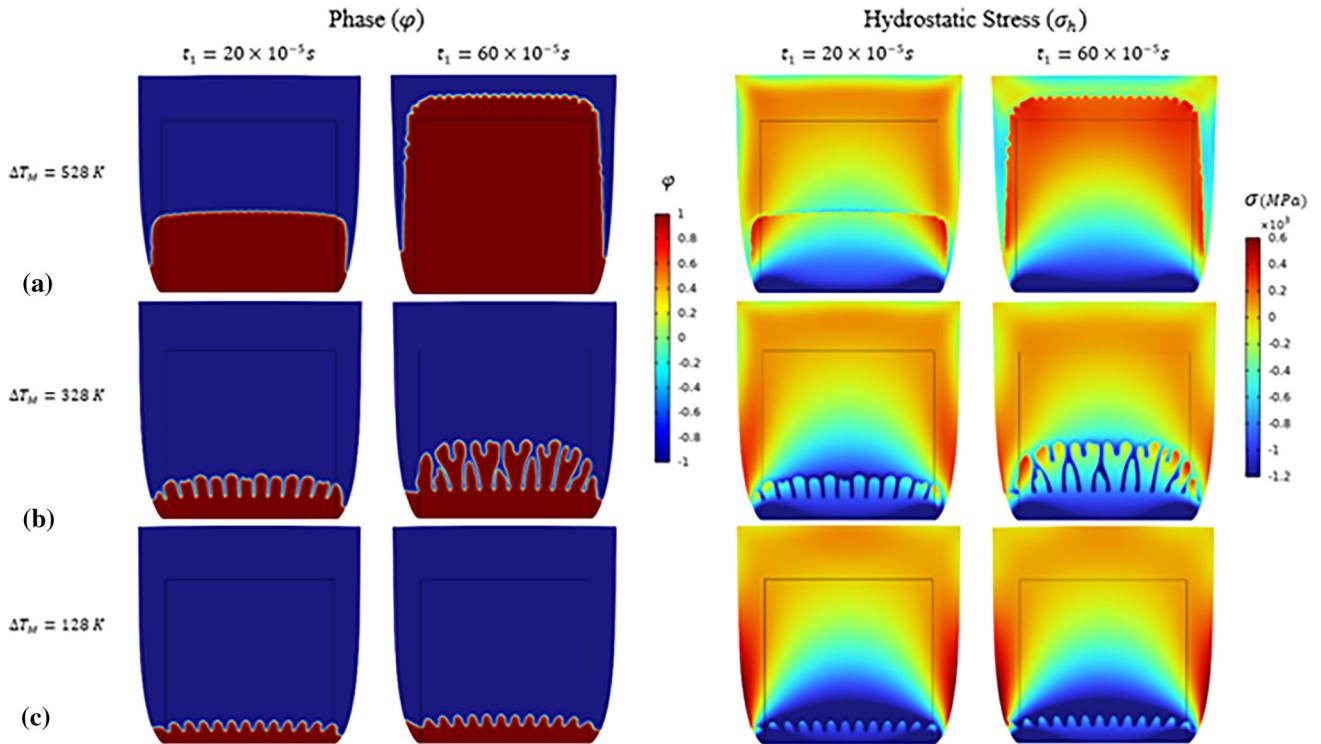


Fig. 8 Evolution for the microstructure (φ) and the corresponding stress for different undercooling magnitudes of (a) 528 K, (b) 328 K and (c) 128 K

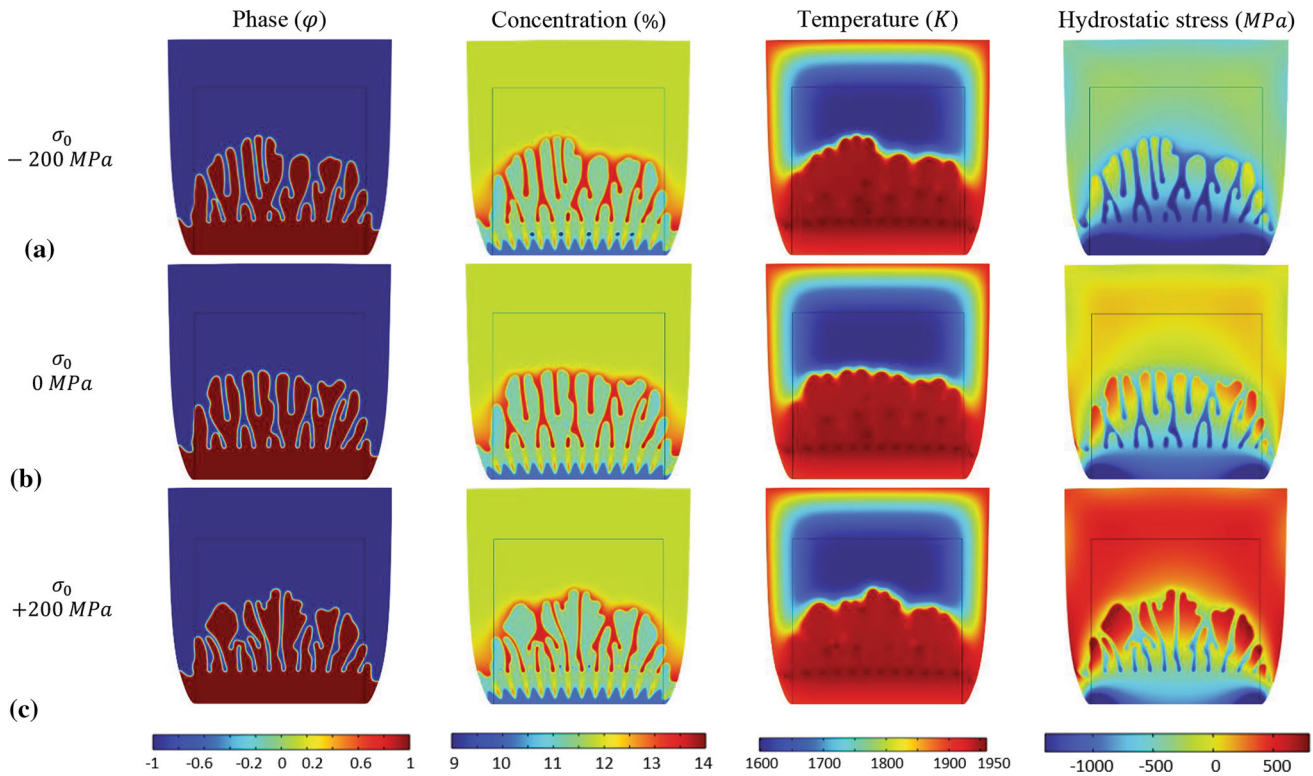


Fig. 9 The microstructure (phase), concentration, temperature and stress field for hydrostatic loadings of $\sigma_0 = -200$ (a), 0 (b) and 200MPa (c) at $t_1 = 100 \times 10^{-5}s$

significance in morphology and kinetics can be found for much larger applied stresses but they are not often used in solidification in laser processes. Note that the main role of mechanics on solidification comes from the huge inelastic strains which creates significant internal stresses. This can be more pronounced in the presence of impurities which, due to their different properties, lead to high heterogeneity in field variables such as stress and notably change the morphology and kinetics. To examine this, the same problem is considered as above but a circular inclusion is included in the sample, as shown in Fig. 10.

Inclusions are one of the common defects seen in AM processes. For Ti6Al4V, Al_2O_3 is known as one of the possible inclusions; thus, it is considered for the current simulation. The thermo-physical properties of Al_2O_3 with the diameter of $5\mu m$ is given in Table 3 (Ref 44).

Since solidification is not considered for the inclusion, the phase parameter φ is not defined in the inclusion. Also, the concentration c is not applicable for this region. Thus, Eqs.17 and 18 are solved (and the phase parameter φ and the concentration c are shown) over the sample except for the inclusion region (Fig. 10). However, elasticity equations and heat conduction equation are solved for the entire sample including the inclusion. Hence, stress and temperature field for the entire sample can be shown. As shown in Fig.10, the inclusion remarkably changes the morphology compared to the

sample without inclusion (Fig. 2) and leads to a higher heterogeneity. In fact, a directional, higher temperature gradient appears toward the inclusion surface which changes the solidification orientation toward the inclusion. The inclusion region shows a more uniform temperature due to the lack of $\frac{L}{2c_p} \frac{\partial \varphi}{\partial t}$ in its heat conduction equation. Higher elastic modulus for the inclusion also causes a higher hydrostatic stress within the inclusion which decreases when solidification passes through it.

4. Conclusion

In this paper, a mechanics based phase-field model at the microscale is introduced for microstructure evolution during solidification which consists of Allen–Cahn, Cahn–Hilliard, heat and elasticity equations. The introduced elastic energy allows for volumetric inelastic strains due to melting/solidification as well as inelastic surface stress and consequently, residual stresses during solidification and the relevant deformation can be captured. Examples of columnar growth are studied where the suppressive effect of elastic driving forces and the reduction in solidification rate, mainly due to the volumetric inelastic strains, on solidification were revealed while the inelastic surface stress did not show a remarkable

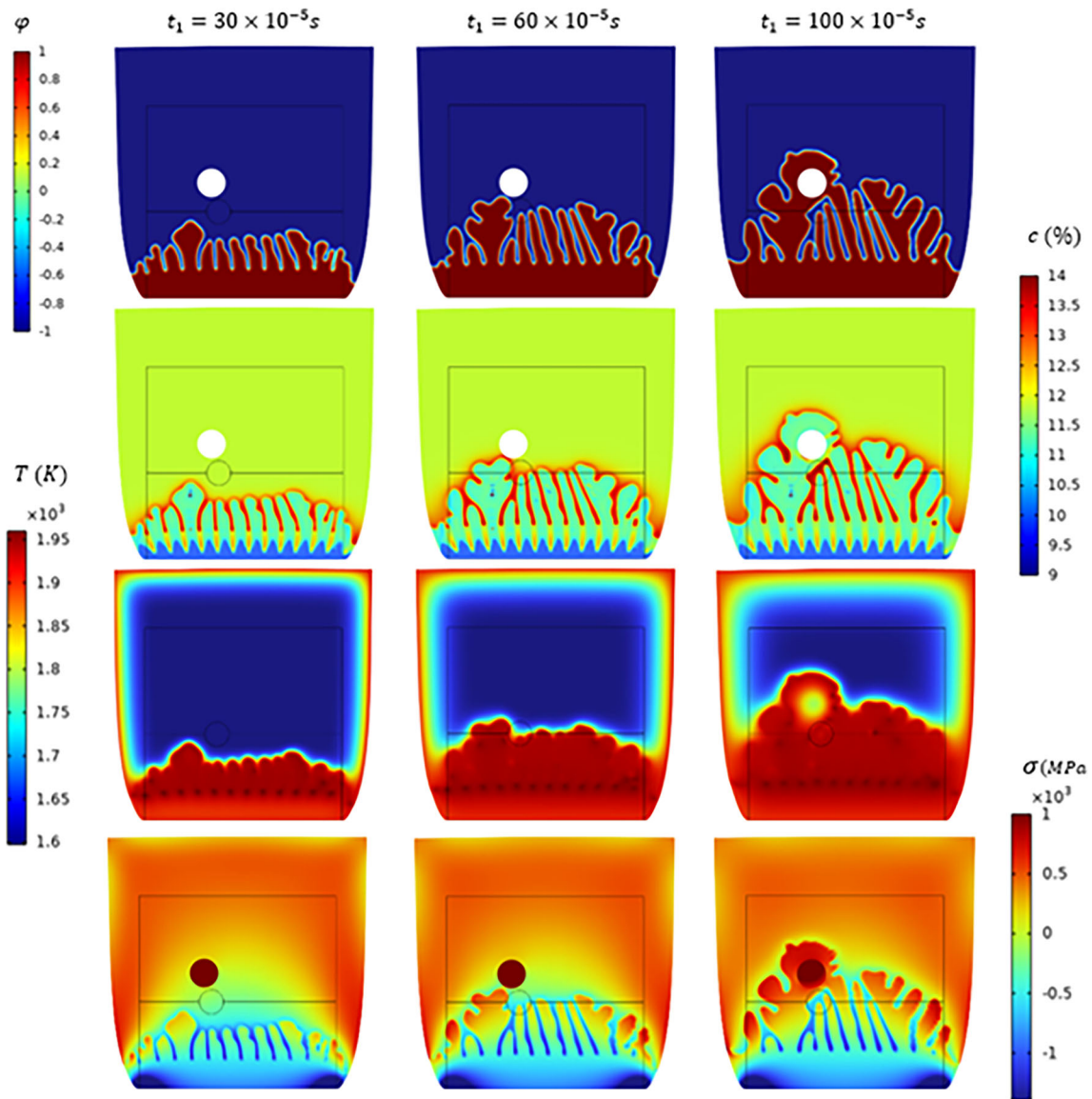


Fig. 10 The evolution of the microstructure, concentration, temperature and stress in the presence of an inclusion

Table 3 Thermo-physical properties of Al_2O_3 (Ref 45, 46)

Parameter	Unit	Value
Elastic modulus	GPa	380
Poisson's ratio	...	0.22
Density	kg/m^3	3900
Thermal expansion coefficient	K^{-1}	$8.2\text{e-}6$
Lewis number	...	1

effect on the solidification rate. Anisotropy was also affected by stresses. Also, due to the negative volumetric transformation strain of solidification, the solidified regions were shrunk and represent positive stress; while the neighboring melt regions were expanded and represented negative stress. The thermal strain was also included and the relevant simulations showed that it reduces the effect of volumetric transformation strain and

consequently, the internal stresses near constrained regions are relaxed. The effect of undercooling, as a crucial parameter in determining the microstructure evolution, was investigated. It was shown that increasing the undercooling increases the temperature gradient along the vertical direction and near the interface and solidification rate and significantly changes the morphology of solidified structure, as a homogeneous growth is resolved for larger undercooling while a columnar growth is obtained for smaller undercooling. Solidification was also studied under mechanical loading which showed external loading changes the stress distribution and magnitude and consequently, the morphology. Effect of an inclusion as an impurity on solidification was also investigated. The inclusion region represented a more homogeneous distribution of stress and temperature with different magnitudes compared to the rest of the sample. As result, the inclusion remarkably changed the morphology, creating a directional solidification toward the inclusion.

Acknowledgments

The help of Isfahan University of Technology and Iran national Science Foundation is gratefully acknowledged.

References

1. W.E. Frazier, Metal Additive Manufacturing: A Review, *J. Mater. Eng. Perform.*, 2014, **23**, p 1917–1928
2. D. Herzog, V. Seyda, E. Wycisk and C. Emmelmann, Additive Manufacturing of Metals, *Acta Mater. Mater.*, 2016, **117**, p 371–392
3. W.J. Sames, F.A. List, S. Pannala, R.R. Dehoff and S.S. Babu, The Metallurgy and Processing Science of Metal Additive Manufacturing, *Int. Mater. Rev.*, 2016, **61**, p 315–360
4. L. Wu and J. Zhang, Phase Field Simulation of Dendritic Solidification of Ti-6Al-4V During Additive Manufacturing Process, *JOM*, 2018, **70**, p 2392–2399
5. R.S. Mishra and S. Thapliyal, Design Approaches for Printability-Performance Synergy in Al Alloys for Laser-Powder Bed Additive Manufacturing, *Mater. Des.*, 2021, **204**, p 109640
6. N.S. Bailey, K.-M. Hong and Y.C. Shin, Comparative Assessment of Dendrite Growth and Microstructure Predictions During Laser Welding of Al 6061 via 2D and 3D Phase Field Models, *Comput. Mater. Sci. Mater. Sci.*, 2020, **172**, p 109291
7. S. Sahoo and K. Chou, Phase-Field Simulation of Microstructure Evolution of Ti-6Al-4V in Electron Beam Additive Manufacturing Process, *Addit. Manuf. Manuf.*, 2016, **9**, p 14–24
8. C. Tang and H. Du, Phase Field Modelling of Dendritic Solidification Under Additive Manufacturing Conditions, *JOM*, 2022, **74**, p 2996–3009
9. J.H.K. Tan, S.L. Sing and W.Y. Yeong, Microstructure Modelling for Metallic Additive Manufacturing: A Review, *Virtual Phys. Prototyping*, 2020, **15**, p 87–105
10. T.M. Rodgers, J.D. Madison and V. Tikare, Simulation of Metal Additive Manufacturing Microstructures Using Kinetic Monte Carlo, *Comput. Mater. Sci. Mater. Sci.*, 2017, **135**, p 78–89
11. H.L. Wei, J.W. Elmer and T. DebRoy, Three-Dimensional Modeling of Grain Structure Evolution During Welding of an Aluminum Alloy, *Acta Mater. Mater.*, 2017, **126**, p 413–425
12. T. Carozzani, C.-A. Gandin, H. Dignonet, M. Bellet, K. Zaidat and Y. Fautrelle, Direct Simulation of a Solidification Benchmark Experiment, *Metall. Mater. Trans. A*, 2013, **44**, p 873–887
13. X. Li and W. Tan, Numerical Investigation of Effects of Nucleation Mechanisms on Grain Structure in Metal Additive Manufacturing, *Comput. Mater. Sci. Mater. Sci.*, 2018, **153**, p 159–169
14. M. Javanbakht and V.I. Levitas, Athermal Resistance to Phase Interface Motion Due to Precipitates: A Phase Field Study, *Acta Mater. Mater.*, 2023, **242**, p 118489
15. V.I. Levitas, M. Javanbakht, Phase-field approach to martensitic phase transformations: effect of martensite–martensite interface energy, 2011, **102**, pp. 652–665
16. A.V. Idesman, V.I. Levitas and E. Stein, Elastoplastic materials with martensitic phase transition and twinning at finite strains: numerical solution with the finite element method, *Comput. Methods Appl. Mech. Eng.*, 1999, **173**, p 71–98
17. H. Jafarzadeh, G.H. Farrahi, V.I. Levitas and M. Javanbakht, Phase field theory for fracture at large strains including surface stresses, *Int. J. Eng. Sci.*, 2022, **178**, p 103732
18. N. Moelans, B. Blanpain and P. Wollants, Quantitative analysis of grain boundary properties in a generalized phase field model for grain growth in anisotropic systems, *Phys. Rev. B*, 2008, **78**, p 024113
19. E. Bakhtiyari, M. Javanbakht and M. Asle Zaeem, Evolution of edge dislocations under elastic and inelastic strains: a nanoscale phase-field study, *Math. Mech. Solids*, 2023, **1081**, p 2865
20. V.I. Levitas and M. Javanbakht, Phase field approach to interaction of phase transformation and dislocation evolution, *Appl. Phys. Lett.*, 2013, **102**, p 251904
21. M. Javanbakht and M.S. Ghaedi, Phase field approach for void dynamics with interface stresses at the nanoscale, *Int. J. Eng. Sci.*, 2020, **154**, p 103279
22. J.C. Ramirez, C. Beckermann, A. Karma and H.J. Diepers, Phase-field modeling of binary alloy solidification with coupled heat and solute diffusion, *Phys. Rev. E*, 2004, **69**, p 051607
23. B. Echebarria, R. Folch, A. Karma and M. Plapp, Quantitative Phase-Field Model of Alloy Solidification, *Phys. Rev. E*, 2004, **70**, p 061604
24. R. Acharya, J.A. Sharon and A. Staroselsky, Prediction of Microstructure in Laser Powder Bed Fusion Process, *Acta Mater. Mater.*, 2017, **124**, p 360–371
25. J. Berry, A. Perron, J.-L. Fattebert, J.D. Roehling, B. Vrancken, T.T. Roehling et al., Toward Multiscale Simulations of Tailored Microstructure Formation in Metal Additive Manufacturing, *Mater. Today*, 2021, **51**, p 65–86
26. K. Karayagiz, L. Johnson, R. Seede, V. Attari, B. Zhang, X. Huang et al., Finite Interface Dissipation Phase Field Modeling of Ni–Nb Under Additive Manufacturing Conditions, *Acta Mater. Mater.*, 2020, **185**, p 320–339
27. L.-X. Lu, N. Sridhar and Y.-W. Zhang, Phase Field Simulation of Powder Bed-Based Additive Manufacturing, *Acta Mater. Mater.*, 2018, **144**, p 801–809
28. D. Tourret and A. Karma, Growth Competition of Columnar Dendritic Grains: A Phase-Field Study, *Acta Mater. Mater.*, 2015, **82**, p 64–83
29. J. Park, J.-H. Kang and C.-S. Oh, Phase-Field Simulations and Microstructural Analysis of Epitaxial Growth During Rapid Solidification of Additively Manufactured AlSi10Mg Alloy, *Mater. Des.*, 2020, **195**, p 108985
30. M. Yang, L. Wang and W. Yan, Phase-Field Modeling of Grain Evolutions in Additive Manufacturing from Nucleation, Growth, to Coarsening, *npj Comput. Mater.*, 2021, **7**, p 56
31. Z. Zhang, X.X. Yao and P. Ge, Phase-Field-Model-Based Analysis of the Effects of Powder Particle on Porosities and Densities in Selective Laser Sintering Additive Manufacturing, *Int. J. Mech. Sci.*, 2020, **166**, p 105230
32. P.W. Liu, Z. Wang, Y.H. Xiao, R.A. Lebensohn, Y.C. Liu, M.F. Horstemeyer et al., Integration of Phase-Field Model and Crystal Plasticity for the Prediction of Process-Structure-Property Relation of Additively Manufactured Metallic Materials, *Int. J. Plast.*, 2020, **128**, p 102670
33. J.-Q. Li and T.-H. Fan, Phase-Field Modeling of Metallic Powder-Substrate Interaction in Laser Melting Process, *Int. J. Heat Mass Transf.*, 2019, **133**, p 872–884
34. V.I. Levitas and K. Samani, Coherent Solid/Liquid Interface with Stress Relaxation in a Phase-Field Approach to the Melting/Solidification Transition, *Phys. Rev. B*, 2011, **84**, p 140103
35. M. Javanbakht, S.S. Eskandari and M. Silani, Surface Induced Melting of Long Al Nanowires: Phase Field Model and Simulations for Pressure Loading and Without It, *Nanotechnology*, 2022, **33**, p 425705
36. V.I. Levitas and M. Javanbakht, Surface Tension and Energy in Multivariant Martensitic Transformations: Phase-Field Theory, Simulations, and Model of Coherent Interface, *Phys. Rev. Lett.*, 2010, **105**, p 165701
37. A. Safdar, L.Y. Wei, A. Snis and Z. Lai, Evaluation of Microstructural Development in Electron Beam Melted Ti-6Al-4V, *Mater. Charact. Charact.*, 2012, **65**, p 8–15
38. S. Ghosh, K. McReynolds, J.E. Guyer and D. Banerjee, Simulation of Temperature, Stress and Microstructure Fields During Laser Deposition of Ti-6Al-4V, *Modell. Simul. Mater. Sci. Eng.*, 2018, **26**, p 075005
39. B. Radhakrishnan, S. Gorti and S.S. Babu, Phase Field Simulations of Autocatalytic Formation of Alpha Lamellar Colonies in Ti-6Al-4V, *Metall. Mater. Trans. A*, 2016, **47**, p 6577–6592
40. K.C. Mills, Ti: Ti-6 Al-4 V (IMI 318), in *Recommended Values of Thermophysical Properties for Selected Commercial Alloys*, ed: Woodhead Publishing, 2002
41. L. Nastac, Solute Redistribution, Liquid/Solid Interface Instability, and Initial Transient Regions During the Unidirectional Solidification of Ti-6-4 and Ti-17 Alloys, *TMS Annu. Meet.*, 2012, **15**, p 123–130

42. J. Ba, X.H. Zheng, R. Ning, J.H. Lin, J. Qi, J. Cao, *et al.* C/SiC Composite-Ti6Al4V Joints Brazed with Negative Thermal Expansion ZrP2WO12 Nanoparticle Reinforced AgCu Alloy. *J. Eur. Ceram. Soc.* 2018, **39**
43. A. Fallahnejad, E. Barchiesi, M. Javanbakht, A.A.S. Nami, Investigating the Effect of Nanovoid Inelastic Surface Stress and the Austenite–Martensite Interface Inelastic Stress on the Martensitic Growth at the Nanovoid Surface. *Contin. Mech. Thermodyn.* 2023
44. Q. Huang, N. Hu, X. Yang, R. Zhang and Q. Feng, Microstructure and Inclusion of Ti-6Al-4V Fabricated By Selective Laser Melting, *Front. Mater. Sci.*, 2016, **10**, p 428–431
45. C. Piconi, 1.105—Alumina, in *Comprehensive Biomaterials*, P. Ducheyne, Ed., ed Oxford: Elsevier, 2011, pp. 73–94
46. D. Dixit, R. Pal, G. Kapoor, M. Stabenau, 6-Lightweight composite materials processing, in *Lightweight Ballistic Composites (Second*

Edition), A. Bhatnagar, Ed., ed: Woodhead Publishing, 2016, pp. 157–216

Publisher's Note Springer Nature remains neutral with regard to jurisdictional claims in published maps and institutional affiliations.

Springer Nature or its licensor (e.g. a society or other partner) holds exclusive rights to this article under a publishing agreement with the author(s) or other rightsholder(s); author self-archiving of the accepted manuscript version of this article is solely governed by the terms of such publishing agreement and applicable law.